MODELING AND DESIGN OF AN LLC RESONANT CONVERTER FOR A WIDE VOLTAGE CONVERSION RATIO APPLICATIONS

BY

ANUJ MAHESHWARI

THESIS

Submitted in partial fulfillment of the requirements
for the degree of Master of Science in Electrical and Computer Engineering
in the Graduate College of the
University of Illinois Urbana-Champaign, 2022

Urbana, Illinois

Adviser:

Assistant Professor Arijit Banerjee

ABSTRACT

LLC Resonant converters provide soft-switching capabilities enabling high switching frequencies and high efficiency. A low-quality factor design operating below resonant frequency is preferred for wide voltage-gain applications to reduce the required range of operating frequencies. Phase-shift modulation can be used in conjunction with frequency modulation to further narrow the operating frequency range. A first harmonic analysis-based approach has high inaccuracies in estimating capacitor voltage, inductor current, and voltage gain, which are critical parameters to design the converter and estimate the losses when phase-shift modulation is employed. This thesis presents a state-plane-based modeling framework to accurately analyze the converter when both frequency and phase-shift modulation are used. The proposed model is then used to highlight the power density versus efficiency trade-off obtained by utilizing phase shift as an additional control variable for an electric vehicle battery charging application. The accuracy of the model is verified by experiments on a 10kW SiC-based prototype. Two converters are designed using the trade-off curve, one employing only frequency modulation and the other using both frequency and phase-shift modulation. These two converters achieve the same efficiency over the constant current battery charging mode but, the addition of phase-shift modulation reduces the transformer's size by 22% and its weight by 28%.

To my parents, for their love and support.

ACKNOWLEDGMENTS

First and foremost, I thank my family for their unlimited love, support, encouragement, and inspiration in my career. It would be impossible for me to go through this journey without them. Being so far away from them has not always been easy but they have continued to have their faith in me, motivate me for further success, and always believe in me.

I do appreciate my advisor, Professor Arijit Banerjee, for providing me with an amazing opportunity to study and research at the University of Illinois at Urbana-Champaign. His knowledge, passion, guidance, and support have always inspired and motivated me to move forward. No matter what I ask, he is always there to support me. Apart from his enthusiastic support for my research, watching him teach in classes with such passion is inspiring.

I would like to express special thanks to Furkan Karakaya for his PCB design and continuous discussions. I also appreciate Patrick Wang and Omkar Kulkarni for their contributions to this project. Moreover, I thank Debranjan Mukherjee, Shivang Agrawal, Bonhyun Ku and Elie Libbos for their endless support and help on my research and experimental setup from the beginning of my graduate study. Finally, I would like to thank Dr. John Donnal for his continuous support and input on this project.

I would like to thank the Office of Naval Research, Advanced Research Projects Agency - Energy, and the Grainger Center for Electric Machinery and Electromechanics at the University of Illinois Urbana-Champaign for supporting this research.

I am grateful to the Power and Energy Systems Research Group students and staff. I am thankful to all the faculties in the power group and faculties who taught the courses I took as a student at UIUC. I consider myself extremely lucky to have the opportunity to learn from people who are the best in their fields. Power Group students are amazing co-workers and friends. They made my life as a graduate student enjoyable and gave me special

moments and memories both inside and outside of school. I am grateful to Kevin Colravy for his experimental and safety support in the laboratory. I thank Joyce Mast for her support in professional writing. I want to thank the ECE Machine Shop experts and ECE Open Lab for their regular help.

I perceive the opportunity to do my MS at UIUC as a big milestone in my career development. I will strive to use the skills and knowledge gained here in the best possible way, and I will continue to work on improving them, in order to attain my desired career objectives.

TABLE OF CONTENTS

LIST OF TABLES

LIST OF FIGURES

CHAPTER 1

INTRODUCTION

An LLC series resonant dc-dc converter, shown in Fig. 1.1, is an attractive solution for the dc-dc conversion stage in many applications including battery charging, solar energy harvesting, and LED driver due to its high efficiency, high power density, and low electromagnetic interference (EMI) over a wide load range [1–8]. The output voltage is typically regulated using frequency modulation [9–13]. Applications that have to accommodate a wider range of voltage conversion ratios need a wider operating frequency range. For example, in a typical battery charging application for an electric vehicle (EV) with a 400V input dc bus, the conversion ratio varies approximately between 0.65 and 1 for a 400V battery pack depending on the battery state of charge [15]. This requirement results in two consequences. First, the optimization of magnetic components becomes challenging, thereby sacrificing power density. Further, the circulating current increases at lower frequencies reducing the converter efficiency.

Adding phase-shift modulation as another control variable reduces the required switching frequency range to achieve an identical voltage conversion ratio. However, an accurate estimation of the state variables is required at all operating conditions to accurately assess the power density versus efficiency trade-off during the design process. For example, [16–19] propose using phase-shift modulation but employ first harmonic approximation (FHA) to design the converter. An FHA-based approach becomes highly inaccurate when the phase-shift modulation is used for a converter with a low-quality factor (Q) operating in discontinuous conduction mode (DCM). Figure 1.2 illustrates the discrepancy between an FHA-based estimation (shown in blue dashed lines) of the capacitor peak voltage and inductor rms current versus their simulated values (shown in solid red lines) using the circuit in Fig. 1.1. DCM is preferred because of the zero current switching of the secondary-side diodes [9, 20], thereby reducing the overall loss. A low Q is desirable to de-

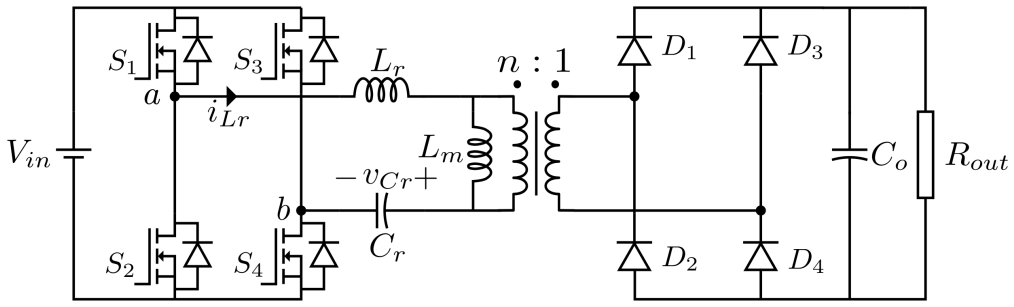

Figure 1.1: Full bridge LLC resonant converter

crease the energy storage requirement in the resonant tank, thus increasing the power density.

Instead of FHA, [21–23] use explicit time-domain equations to estimate the state variables. While this approach improves accuracy and is useful to simulate particular operating conditions, it makes the optimization challenging over a wide design space. Reference [24, 25] models the LLC converter under phase-shift modulation using a state-space approach but restricts the modeling to continuous conduction mode. Although [26–28] model the converter in DCM mode, these ignore the magnetizing inductance when operating with phase-shift modulation. Similarly, [29] assumes magnetizing inductance as infinite for part of the analysis. This leads to discrepancies between the model and the simulation. An open question remains: How do we accurately model and design a low-Q LLC series resonant converter operating in discontinuous conduction mode without neglecting the magnetizing inductance and allowing phase-shift modulation?

The key contribution of this thesis is a state-plane-based approach to model a low-Q, LLC series resonant converter to estimate the capacitor peak voltage requirement and the inductor rms current under phase-shift and frequency modulation, without neglecting the magnetizing inductance. Instead of explicitly solving differential equations for each operating mode, the entire steady-state operation is captured via the capacitor charge-voltage relationship, input/output energy balance, and time periodicity. These three considerations enable the creation of a modeling framework with operating frequency and phase-shift as inputs and state trajectories and voltage conversion ratio as outputs. The proposed framework is next used to capture the trade-off between a converter's efficiency and power density for an EV battery

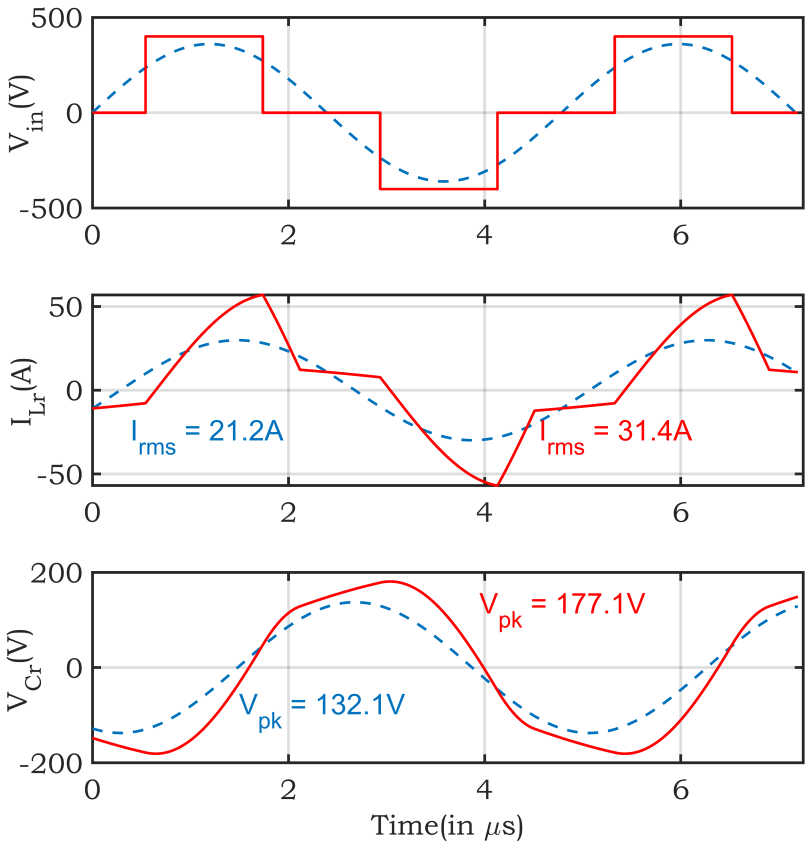

Figure 1.2: Waveforms of state variables using FHA (blue dashed lines) and circuit simulation in PLECS (solid red lines) for $L_r = 3.5\mu H$, $C_r = 180nF$, $f_{sw} = 200kHz$, $R_{out} = 16\Omega$, $V_{in} = 400V$, and phase-shift $= \pi/2$.

charging application with a voltage conversion ratio of 0.65 to 1 and a maximum output voltage of 400V. The time-weighted average efficiency approach is used to optimize the design over the constant current (CC) charging mode. The converter employing both frequency and phase-shift as control variables reduce the transformer's size by 22%, weight by 28%, and the peak energy stored in the resonant capacitor by 1.7x, while incurring the same energy loss over the 20%–80% charging cycle and incurring 36% less loss over the 80%–100% charging cycle compared to an only frequency modulated LLC converter.

The rest of the thesis is organized as follows. Chapter 2 discusses the preferred region of operation for the LLC converter in a wide voltage range application. Chapter 3 presents the generalized state plane approach for a

series LLC converter. Chapter 4 discusses the optimization framework to design the LLC converter. Chapter 5 gives the experimental and simulation results to verify the proposed model. Chapter 6 concludes the thesis.

CHAPTER 2

PREFERABLE OPERATING REGION OF AN LLC CONVERTER FOR A WIDE-VOLTAGE CONVERSION RATIO

This chapter shows the advantages of designing and operating an LLC series resonant converter in DCM with a low Q to achieve a wide voltage conversion ratio. Although the FHA-based approximation is inaccurate under these conditions, the discussion below uses this well-known method to explain the need for an accurate model in this operating region.

The voltage gain (V_{out}/V_{in}) of an LLC resonant converter assuming FHA is given by [30]:

$$M(f_n, k, Q) = \frac{k}{\sqrt{(1 + k - \frac{1}{f_n^2})^2 + Q^2k^2(f_n - \frac{1}{f_n})^2}} \tag{2.1}$$

where f_n is the normalized switching frequency (f_{sw}/f_{r1}), k is the ratio of magnetizing inductance, L_m, to series inductance, L_r, and Q is defined by

$$Q = \frac{Z_0}{R_{eq}} \tag{2.2}$$

where

$$Z_0 = \sqrt{\frac{L_r}{C_r}} \text{ and } R_{eq} = \frac{8n^2R_{load}}{\pi^2} \tag{2.3}$$

$n:1$ is the transformer turns ratio, C_r is the series capacitance, R_{load} is the load resistance. An LLC resonant converter has two resonant frequencies and these are given by

$$f_{r1} = \frac{1}{2\pi\sqrt{L_rC_r}} \text{ and } f_{r2} = \frac{1}{2\pi\sqrt{(k+1)L_rC_r}} \tag{2.4}$$

Figure 2.1 illustrates the possible operating regions using an example k of seven for a range of Q to achieve the same voltage conversion ratio. In order to ensure zero voltage switching (ZVS) of the MOSFETs, the converter must operate in the inductive region which implies normalized switching fre-

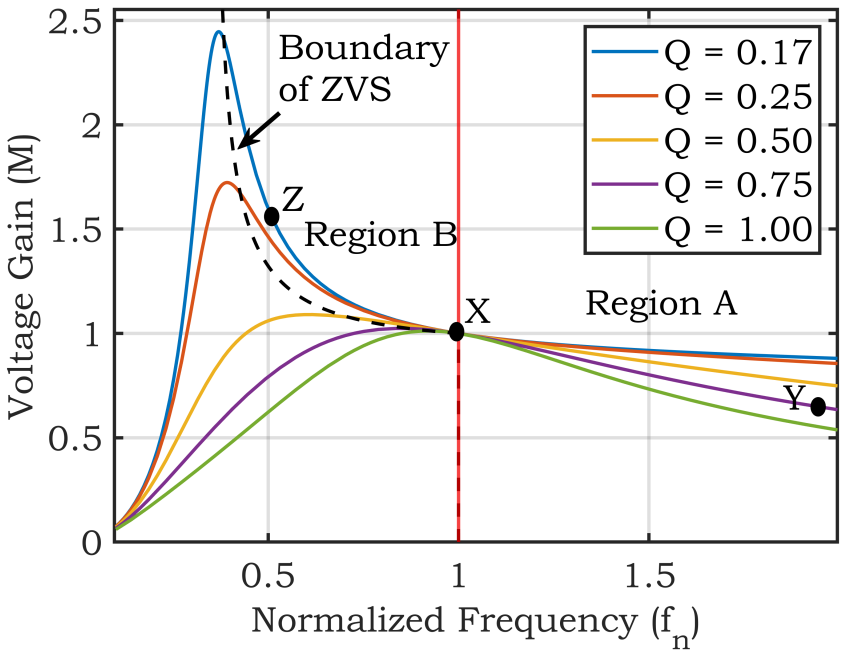

Figure 2.1: Voltage gain of an LLC resonant converter using FHA for k = 7.

quencies greater than f_{r2}. In Region A, the converter always operates at frequencies above the resonant frequency f_{r1}. A high Q design is necessary to limit the operating frequency range while achieving a wide voltage gain. For example, to achieve a conversion ratio varying from 0.65 to 1 and $f_{n\_max}/f_{n\_min} = 1.94$, the required Q is 0.75. The operating range for this design is marked by points X and Y on the figure. Alternatively, designing the converter to operate in Region B would call for a low Q design. For the same conversion ratio and same f_{n_max}/f_{n_min}, the required Q is 0.17 in this region. The operating region is marked by points X and Z. As the quality factor is a measure of stored energy, a high Q design translates into a bulkier resonant tank. Moreover in Region A, the secondary-side rectifiers lose zero current switchings (ZCS) decreasing the overall efficiency. Therefore, Region B is preferred to maximize the power density and efficiency for a wide voltage conversion ratio.

However, using an FHA-based model to capture the inductor current and capacitor voltage waveforms in Region B leads to inaccuracies, as discontinuous conduction of the rectifier diodes along with a lower Q, makes them far from sinusoidal. The inaccuracies are further increased when phase-shift

modulation is used to reduce the operating frequency range, as shown in Fig. 1.2. These are the critical variables to understand the converter's underlying power density versus efficiency trade-off. Inductor rms current is important as it is a key indicator of efficiency. In the presence of primary-side ZVS and secondary-side ZCS, the switching losses are insignificant. The converter losses primarily occur as conduction losses in the MOSFET's on-state resistance and capacitor's equivalent series resistance (ESR) along with winding losses in the transformer and inductor. The capacitor peak voltage dictates the energy-storage requirement, thereby influencing the capacitor volume.

Maintaining ZVS throughout the operating region is necessary for high efficiency. ZVS requires a minimum circulating current during the switch transition's dead time and this current is dictated by the magnetizing inductance. Any analysis ignoring the magnetizing inductance will not only lose the information about ZVS but will also give inaccurate estimates for state variables, as the current going into magnetizing inductance will be neglected. Therefore, a low Q LLC converter operating in the below resonant frequency region with phase-shift modulation requires a better modeling approach for accurate converter design.

CHAPTER 3

STATE-PLANE ANALYSIS OF LLC RESONANT CONVERTER

This chapter presents a state-plane-based model that accurately calculates the voltage gain, inductor rms current, and capacitor peak voltage as a function of operating frequency, phase shift, passive components, magnetizing inductance, and load current. Additionally, the model also captures the switching current at the switching instants to ensure ZVS for the entire operating range. The following assumptions are considered:

1. MOSFETs and diodes are treated as ideal switches
2. Transformer, inductor, and capacitor are lossless
3. Output voltage ripple is negligible
4. Converter is in periodic steady state

3.1 Basics of State Plane Approach

The state plane approach is essentially a geometric way of solving differential equations. In this technique, the state variables are plotted as they evolve with time. In the particular case of the LLC resonant converter, there are two state variables — the resonant inductor current and the resonant capacitor voltage. The state plane for two fundamental circuit states of the LLC resonant converter is described next.

3.1.1 State Plane when a DC voltage is applied to an LC tank

The differential equations governing the state variables when a dc voltage is applied across an LC resonant tank, as shown in Fig. 3.1, is given by:

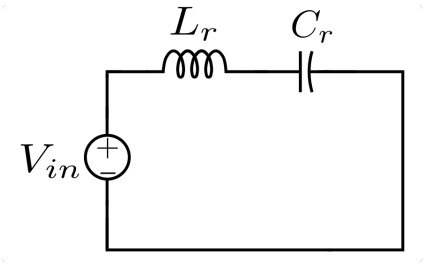

Figure 3.1: Circuit diagram of LC tank

$$i_{Lr} = C_r \frac{dv_{Cr}}{dt} \tag{3.1}$$

$$L_r \frac{di_{Lr}}{dt} + v_{Cr} = V_{dc} \tag{3.2}$$

Differentiating (3.2), and substituting dv_{Vr}/dt in 3.1, we get a second order differential equation given by

$$i_{Lr} = -C_r L_r \frac{d^2 i_{Lr}}{dt^2} => \frac{d^2 i_{Lr}}{dt^2} = -\omega_0^2 i_{Lr} \tag{3.3}$$

where ω_0^2 is equal to $1/\sqrt{L_r C_r}$. The solution of the differential equation with the initial conditions

$$i_{Lr}(0) = 0 \tag{3.4}$$

and

$$v_{Cr}(0) = 0 \tag{3.5}$$

is given by

$$i_{Lr} = I_0 sin(\omega_0 t) \tag{3.6}$$

and

$$v_{Cr} = V_{dc}(1 - cos(\omega_0 t)) \tag{3.7}$$

where I_0 is given by V_{dc}/Z_0 where Z_0 is called the characteristic impedance of the resonant tank given by

$$Z_0 = \sqrt{\frac{L_r}{C_r}} = \omega_0 L_r = \frac{1}{\omega_0 C_r} \tag{3.8}$$

Using the identity, $sin^2(\theta) + cos^2(\theta) = 1$ and combining (3.7) and (3.8)

$$(\frac{i_{Lr}}{I_0})^2 + (1 - \frac{v_{Cr}}{V_{dc}})^2 = 1 \tag{3.9}$$

If we normalize the inductor current by I_0 and capacitor voltage by V_{dc}, (3.9)

becomes

$$j_l^2 + (1 - m_c)^2 = 1 \tag{3.10}$$

where j_l and m_c are normalized inductor current and capacitor voltage respectively. (3.10) is an equation of a circle centered at (1,0) and radius 1. Therefore, the state plane when a DC voltage is applied to an LC tank is given by a circle as shown in fig. 3.2. The center is located at (1,0) because the normalization voltage is equal to the voltage across the tank. In a more general case, the center will be given by ($V_{\text{across the LC tank}}/V_{normalization}$, 0).

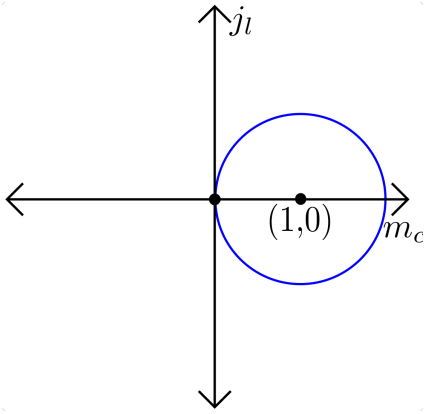

Figure 3.2: State plane of LC tank under DC excitation

3.1.2 State Plane when a DC voltage is applied to an LLC tank

The differential equations governing the state variables when a dc voltage is applied across an LC resonant tank, as shown in Fig. 3.3, is given by:

$$i_{Lr} = C_r \frac{dv_{Cr}}{dt} \tag{3.11}$$

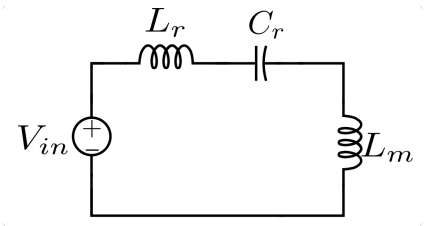

Figure 3.3: Circuit diagram of LLC tank

$$(L_r + L_m)\frac{di_{Lr}}{dt} + v_{Cr} = V_{dc} \Rightarrow L_r(1 + k)\frac{di_{Lr}}{dt} + v_{Cr} = V_{dc} \tag{3.12}$$

where k = L_m/L_r. Differentiating (3.12), and substituting dv_{Vr}/dt in 3.11, we get a second order differential equation given by

$$i_{Lr} = -C_r L_r(1 + k)\frac{d^2 i_{Lr}}{dt^2} \Rightarrow \frac{d^2 i_{Lr}}{dt^2} = -\frac{\omega_0^2}{1 + k} i_{Lr} \tag{3.13}$$

The solution of the differential equation with the initial conditions

$$i_{Lr}(0) = 0 \tag{3.14}$$

and

$$v_{Cr}(0) = 0 \tag{3.15}$$

is given by

$$i_{Lr} = \frac{I_0}{\sqrt{1+k}} sin(\frac{\omega_0}{\sqrt{1+k}} t) \tag{3.16}$$

and

$$v_{Cr} = V_{dc}(1 - cos(\frac{\omega_0}{\sqrt{1+k}} t)) \tag{3.17}$$

Using the identity, $sin^2(\theta) + cos^2(\theta) = 1$ and combining (3.16) and (3.17)

$$(1+k)(\frac{i_{Lr}}{I_0})^2 + (1 - \frac{v_{Cr}}{V_{dc}})^2 = 1 \tag{3.18}$$

If we normalize the inductor current by I_0 and capacitor voltage by V_{dc}, (3.18) becomes

$$(1+k)j_l^2 + (1 - m_c)^2 = 1 \tag{3.19}$$

which is an equation of an ellipse centered at (1,0) with major axis 1 and minor axis $1/\sqrt{1+k}$. Therefore, the state plane when a DC voltage is applied to an LLC tank is given by an ellipse as shown in fig. 3.4. Due to the addition of L_m, the state plane transforms from a circle to an ellipse. The angular frequency with which the state vector moves within the state plane also reduces by a factor of $\sqrt{1+k}$.

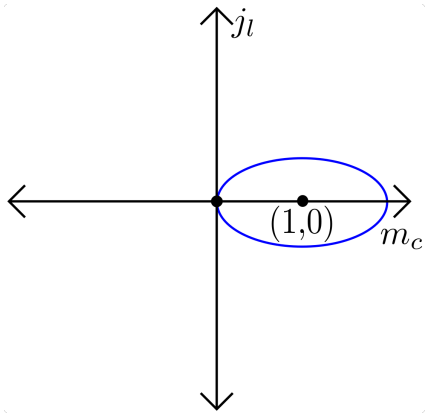

Figure 3.4: State plane of LLC tank under DC excitation

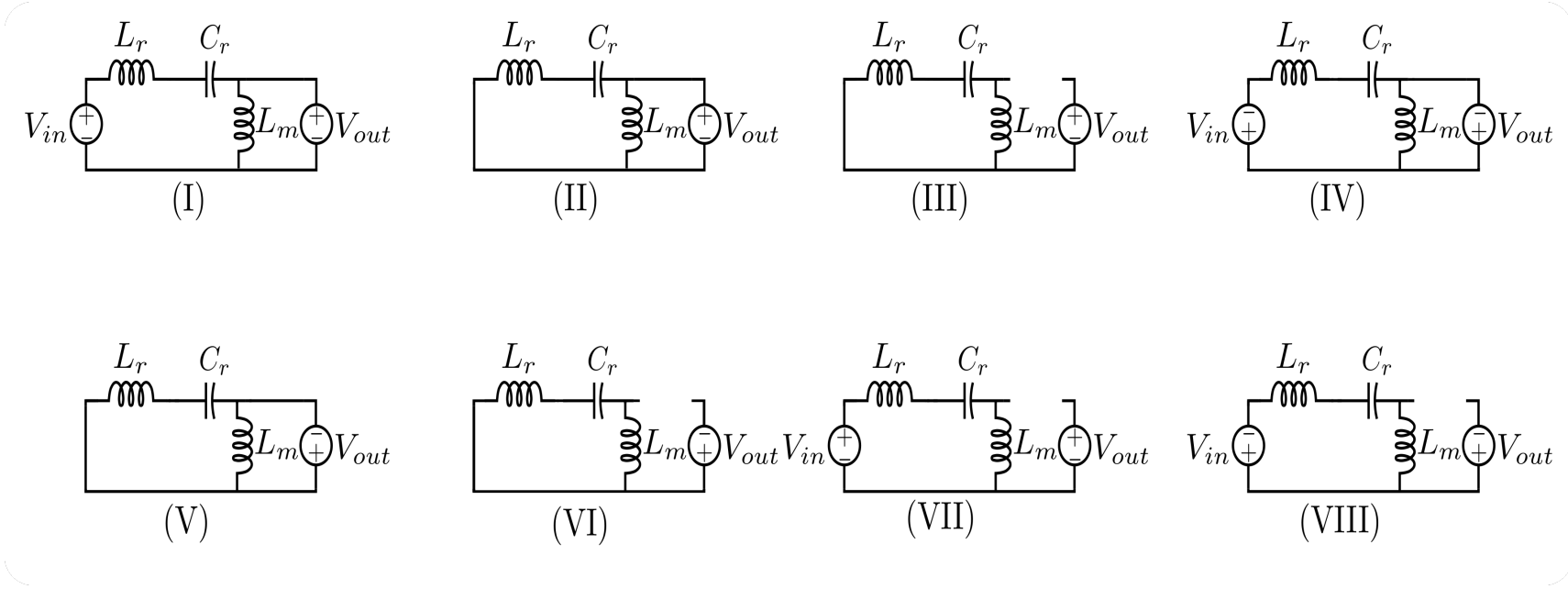

Figure 3.5: Different equivalent circuits of LLC resonant converter depending upon primary side MOSFET and secondary side diode conduction state.

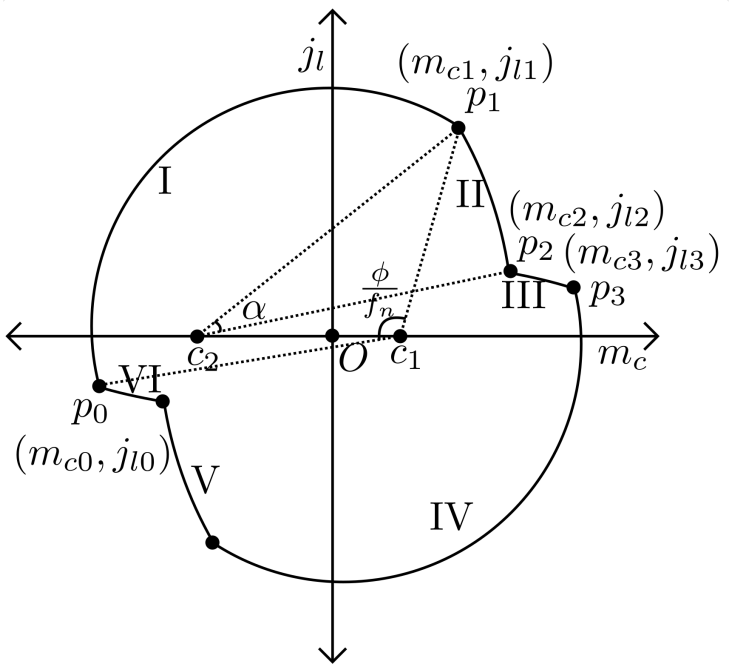

Figure 3.6: State plane for Type I DCM: when the input voltage to the resonant tank is shorted before the diodes stop conducting

3.1.3 State Planes for an LLC resonant tank converters

The state plane of the LLC resonant converter is a combination of arcs of circles and ellipses with varying centers depending upon the voltage across the resonant tank and radius which depends on initial conditions. Figure 3.5 shows the equivalent circuits depending on the MOSFET switching state and diode conduction state when the converter is operating in Region B. Two different DCM modes are possible, depending on the phase shift between the two legs of the full bridge. Type I DCM occurs if the diodes keep conducting when the input to the tank is shorted, and the circuit transitions through I→II→III→IV→V→VI. The resulting state plane is shown in Fig. 3.6. Alternatively, type II DCM occurs if the diodes turn off before the input to the tank is shorted, and the circuit transitions through I→VII→III→IV→VIII→VI. The corresponding state plane is shown in Fig. 3.7. If the phase-shift equals π, which is the case for only frequency modulation, the state plane reduces to Modes I→VII→IV→VIII.

The state plane shown in Fig. 3.6 is the one of interest for the majority of operating conditions, as voltage gain becomes more sensitive at lower phase-shift values. The analysis for this state plane is described next.

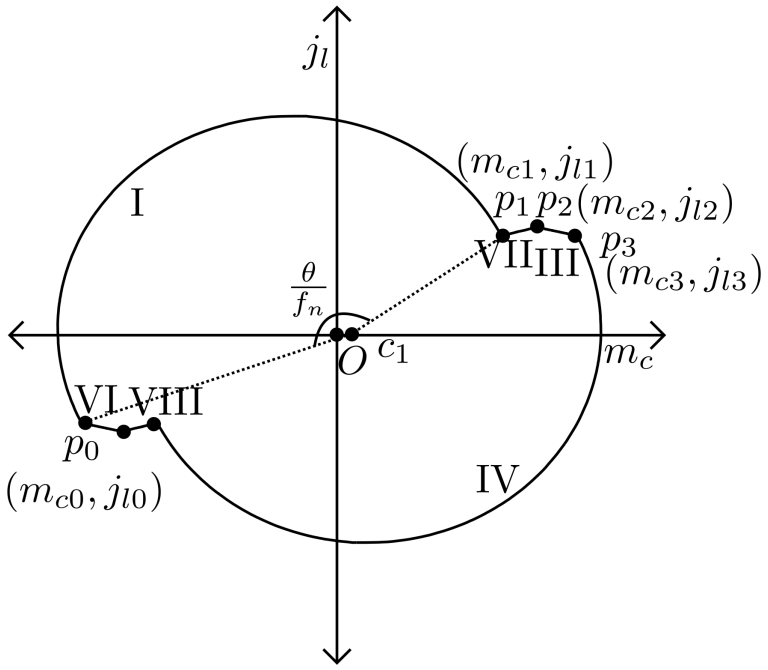

Figure 3.7: State plane for Type II DCM: when the input voltage to the resonant tank is shorted after the diodes stop conducting.

3.2 Type I Discontinuous Conduction Mode

The converter's state plane modeling is carried out in terms of normalized variables. The normalized variables of interest are:

$$\text{Normalized input voltage: } M_{in} = \frac{V_{in}}{V_{in}} = 1 \tag{3.20}$$

$$\text{Normalized output voltage: } M_{out} = \frac{nV_{out}}{V_{in}} = \text{Gain} = M \tag{3.21}$$

$$\text{Normalized capacitor voltage: } m_c = \frac{v_c}{V_{in}} \tag{3.22}$$

$$\text{Normalized inductor current: } j_l = \frac{i_{Lr}}{I_n} \tag{3.23}$$

$$\text{Normalized output current: } J_{out} = \frac{I_{out}}{nI_n} \tag{3.24}$$

$$\text{where } I_n = \frac{V_{in}}{Z_0} \tag{3.25}$$

where V_{in} and V_{out} are average input and output voltage, respectively, v_c and i_l are instantaneous voltage across C_r and current through L_r and $n:1$ is

transformer turns ratio. The different modes shown in Fig. 3.6 occur for the corresponding circuit states shown in Fig. 3.5. In Mode I, when the input voltage to the tank is $M_{in} = 1$ and the diodes D1 and D4 are conducting, which makes the voltage across the magnetizing inductance M, the state trajectory is an arc of a circle with center at $c1 = (1 - M, 0)$. The circle's equation in this mode is given by

$$\text{Mode I: } (m_c - (1 - M))^2 + j_l^2 = r_1^2 \tag{3.26}$$

The initial conditions for the normalized capacitor voltage and inductor current as marked by point p_0 in the state plane are assumed to be (m_{c0}, j_{l0}). The radius r_1 of the circle in Mode I is known in terms of m_{c0}, j_{l0} and M, as p_0 lies on the circle. The converter stays in this mode for a phase duration of phase-shift, ϕ and subtends an angle of ϕ/f_n at the center c_1 during this interval. Mode II begins when the input to the resonant tank is effectively shorted. The diodes D1 and D4 are still conducting and therefore the voltage across the magnetizing branch is M. The state plane is an arc of a circle but with the center at $c_2 = (-M, 0)$. The equation in this mode is given by

$$\text{Mode II: } (m_c - (-M))^2 + j_l^2 = r_2^2 \tag{3.27}$$

The point p_1, which marks the end of Mode I and the beginning of Mode II is equivalent to the vector $(p_0 - c_1)$ rotated by the angle ϕ/f_n in the clockwise direction and is given by

$$\begin{bmatrix} m_{c1} \\ j_{l1} \end{bmatrix} = \begin{bmatrix} m_{c0} - (1 - M) \\ j_{l0} \end{bmatrix} \begin{bmatrix} cos(\frac{\phi}{f_n}) & sin(\frac{\phi}{f_n}) \\ -sin(\frac{\phi}{f_n}) & cos(\frac{\phi}{f_n}) \end{bmatrix} + \begin{bmatrix} 1 - M \\ 0 \end{bmatrix} \tag{3.28}$$

The point p_1, marked as (m_{c1}, j_{l1}), is known in terms of initial conditions and voltage gain from (3.28) and thus the radius r_2 is also known by substituting p_1 in (3.27).

As the inductor current is decreasing in Mode II and the current in the magnetizing branch is rising linearly due to a constant positive voltage across it, the diodes stop conducting when these two become equal. This instance marks the end of Mode II, and the magnetizing inductance L_m joins resonance making the state trajectory an arc of an ellipse. The equation governing the

state trajectory in this mode is

$$\text{Mode III: } m_c^2 + (k+1)j_l^2 = r_3^2 \tag{3.29}$$

The point p_3 is the mirror image of point p_0:

$$p_3 = -p_0 = (-m_{c0}, -j_{l0}) \tag{3.30}$$

The only remaining point of interest on the state plane is p_2. This can be found by calculating the intersection point of the ellipse of Mode III and the circle of Mode II. Thus, all the state trajectories are known in terms of switching frequency, phase-shift, and three unknowns: the converter voltage gain and the initial condition of the state variables (m_{c0}, j_{l0}). The first of the three equations to solve for the unknowns come from the input/output energy balance over a half-switching time period. In normalized form:

$$M_{in} < j_{in} >= M_{out} J_{out} \Rightarrow < j_{in} >= M J_{out} \tag{3.31}$$

$$\text{where } < j_{in} >= \frac{f_n(m_{c1} - m_{c0})}{\pi} \tag{3.32}$$

Equation 3.32 comes from the fact that the average value of the y coordinate in an arc of the circle is given by the difference of x coordinates divided by the angle subtended by the arc at the center, which has been explained in appendix A1.

The second equation comes from the capacitor charge-voltage relationship. During the half-time period comprising Modes I, II, and III, the capacitor charges and its voltage swings from m_{c0} to $-m_{c0}$. The change in capacitor voltage is given by

$$\Delta v_{C_r} = \frac{\Delta q}{C_r} = \frac{< i_{L_r} > T_s}{2C_r} \tag{3.33}$$

where T_s is the switching time period. In normalized form,

$$\Delta m_c = -2m_{c0} = \frac{< j_l > \pi}{f_n C_r} \tag{3.34}$$

The average value of current flowing into the capacitor during this period is

$$< j_l >= J_{out} + < j_{lm} > \tag{3.35}$$

where j_{lm} is the normalized current in the magnetizing inductance and its average over a half-time period is given by

$$< j_{lm} >= \frac{< j_{lm,I-II} > (\phi + f_n\alpha) + < j_{lm,III} > \delta}{\phi + f_n\alpha + \delta} \tag{3.36}$$

where ϕ and $f_n\alpha$ are the phase duration corresponding to Modes I and II respectively, during which $< j_{lm} >$ is linear. δ is the phase duration corresponding to Mode III, when $< j_{lm} >$ is sinusoidal. α is the angle subtended by points p_1 and p_2 at the center c_2, as shown in Fig. 3.6. As j_{l0} is also the starting point of the magnetizing current's linear segment, its average in Modes I and II combined is

$$< j_{lm,I-II} >= \frac{1}{2}(2j_{l0} + \frac{M}{f_n k}(\phi + f_n\alpha)) \tag{3.37}$$

where $M/f_n k$ is the normalized slope. The elliptical state trajectory of Mode III is transformed into a circular trajectory by changing the normalization factor for current from V_{in}/Z_0 to V_{in}/Z_1 where $Z_1 = \sqrt{(L_m + L_r)/C_r}$ to get

$$\delta = \sqrt{k+1} f_n \beta \tag{3.38}$$

where β is the angle subtended by the state-trajectory arc at its center in the Z_1 normalized state plane. Finally, $< j_{lm,III} >$ is given by

$$< j_{lm,III} >= \frac{-m_{c0} - m_{c2}}{\sqrt{k+1}\beta} \tag{3.39}$$

using the same approach as explained in Appendix A.

The third equation comes from the time periodicity. The time at which the state plane starts as a circle from point p_0 and ends as an ellipse at point p_3 is half the total time period. In angular form,

$$f_n(\frac{\phi}{f_n} + \alpha + \sqrt{(k+1)}\beta) = \pi \tag{3.40}$$

Equations (3.31), (3.34) and (3.40) are sufficient to compute the voltage gain, M, and the initial conditions m_{c0} and j_{l0} for a given load current, phase-shift, and switching frequency. Since the equations are transcendental in nature, closed-form solutions are impossible. Matlab function *vpasolve* is

used to numerically solve for the unknowns. Once the unknowns are solved, the current in the magnetizing inductance at the end of Mode I is given by

$$j_{m1} = j_{l0} + \frac{M}{f_n k}\phi \tag{3.41}$$

If $j_{m1} \leq j_{l1}$, the assumption that diodes are conducting at the end of Mode I is true and the converter is in type I DCM. Otherwise, the converter is operating in type II DCM whose analysis is discussed next.

3.3 Type II Discontinuous Conduction Mode

The state variables follow the trajectory, as shown in Fig. 3.7 if the diodes turn off before the inputs are shorted. Mode II is replaced by Mode VII for this state trajectory. The combined phase duration of Modes I and VII is ϕ. Therefore, the phase duration of Mode III, δ, is $\pi - phi$. The underlying principles to obtain the three equations remain the same with some modifications. The equation of the ellipse in Mode VII is given by:

$$\text{Mode VII: } (m_c - 1)^2 + (k+1)j_l^2 = r_7^2 \tag{3.42}$$

Since, δ is known, β can be calculated from (3.38). The point $p_2(m_{c2}, j_{l2})$ which marks the end of Mode VII and the beginning of Mode III is equivalent to vector $(p_3 - O)$ by angle β in the counterclockwise direction and is given by

$$\begin{bmatrix} m_{c2} \\ \sqrt{k+1}j_{l2} \end{bmatrix} = \begin{bmatrix} -m_{c0} \\ -\sqrt{k+1}j_{l0} \end{bmatrix} \begin{bmatrix} cos(\beta) & -sin(\beta) \\ sin(\beta) & cos(\beta) \end{bmatrix} \tag{3.43}$$

As p_2 lies on the ellipse of Mode VII, the semi-major axis of the ellipse, r_7, can be calculated by substituting it in (3.42). The point p_1 is calculated by finding the intersection point of Mode I and Mode VII state trajectories. Now, all the state trajectories are known in terms of switching frequency, phase shift, and the same three unknowns.

$< j_{lm} >$ is given by

$$< j_{lm} >= \frac{< j_{lm,I} > \theta + < j_{lm,VII} > \delta' + < j_{lm,III} > \delta}{\theta + \delta' + \delta} \tag{3.44}$$

where θ/f_n is the phase angle corresponding to Mode I and δ' is the corresponding phase duration for mode VII. It is given by

$$\delta' = \sqrt{k+1} f_n \gamma \tag{3.45}$$

where γ is the angle subtended by the state-trajectory arc at its center in the Z_1 normalized state plane. $< j_{lm,VII} >$ is given by

$$< j_{lm,VII} >= \frac{-m_{c2} - m_{c1}}{\sqrt{k+1}\gamma} \tag{3.46}$$

In this case, the time periodicity equation is

$$f_n(\frac{\theta}{f_n} + \sqrt{(k+1)}(\beta + \gamma)) = \pi \tag{3.47}$$

and the input/output energy balance equation is

$$M_{in} < j_{in} >= M_{out} J_{out} \Rightarrow < j_{in} >= M J_{out} \tag{3.48}$$

$$\text{where } < j_{in} >= \frac{f_n(m_{c2} - m_{c0})}{\pi} \tag{3.49}$$

3.4 Design Parameters

The capacitor peak voltage and inductor rms current are required to evaluate the power density versus efficiency trade-off of the converter. The peak normalized capacitor voltage is the absolute value of the x-intercept of the circular state plane in Mode I. It is given by

$$m_{C,peak} = |(r1 - (1 - M))| \tag{3.50}$$

The inductor rms current in different modes are:

$$\text{Mode I} : j_{l,rms1} = \sqrt{\frac{1}{2}(r_1^2 - \frac{m'_{c0} j'_{l0} - m'_{c1} j'_{l1}}{\frac{\phi}{f_n}})} \tag{3.51}$$

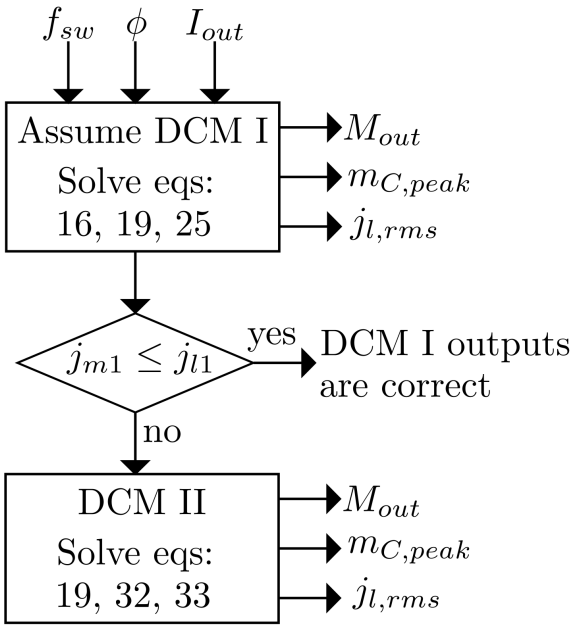

Figure 3.8: Model flowchart for calculating converter gain, capacitor peak voltage, and inductor rms current for given converter parameters: L_r, C_r, L_m, n.

$$\text{Mode II} : j_{l,rms2} = \sqrt{\frac{1}{2}(r_2^2 - \frac{m'_{c1}j'_{l1} - m'_{c2}j'_{l2}}{\alpha})} \tag{3.52}$$

$$\text{Mode III} : j_{l,rms3} = \frac{1}{\sqrt{k+1}}\sqrt{\frac{1}{2}(r_3^2 - \frac{m''_{c2}j''_{l2} - m''_{c3}j''_{l3}}{\beta})} \tag{3.53}$$

Details of these are given in Appendix A2. The prime denotes the variables shifted in the x-axis so that the center of the arcs is at the origin, for instance

$$\begin{bmatrix} m'_{c0} \\ j'_{l0} \end{bmatrix} = \begin{bmatrix} m_{c0} \\ j_{l0} \end{bmatrix} + \begin{bmatrix} (1-M) \\ 0 \end{bmatrix} \tag{3.54}$$

and the double prime denotes the variable shifted in the x-axis so that the center is at the origin after the ellipse-to-circle transformation. The rms value over half the time period is the weighted sum of rms values in different modes:

$$j_{l,rms} = \sqrt{\frac{j_{l,rms1}^2\phi + j_{l,rms2}^2\alpha f_n + j_{l,rms3}^2\beta\sqrt{k+1}f_n}{\pi}} \tag{3.55}$$

The last step in this modeling framework is to establish constraints to

ensure ZVS. The current at the time of the switching instant is given by j_{l0} and ZVS is ensured if

$$j_{l0} \geq \frac{2C_{oss}Z_0}{t_{deadtime}} \tag{3.56}$$

In the case of frequency modulation only, ZVS is ensured if

$$j_{l0} \geq \frac{4C_{oss}Z_0}{t_{deadtime}} \tag{3.57}$$

where C_{oss} is the output capacitance of the MOSFET provided in the device datasheet.

To summarize, this chapter derived a model of an LLC resonant converter operating in Region B under both frequency and phase-shift modulation. Figure 3.8 shows a flowchart of the proposed approach.

CHAPTER 4

LLC RESONANT CONVERTER DESIGN FOR AN EV BATTERY-CHARGING APPLICATION

Electric vehicles typically have a 400V lithium-ion battery pack whose terminal voltage can vary from 260V to 400V, depending upon the battery state of charge. The converter needs to be designed to work efficiently over this entire wide output voltage range. This output voltage regulation range requirement translates to a gain variation of 0.65 to 1 for a 400V dc voltage bus, which is the output of a typical power factor correction (PFC) rectifier used in charging applications. The design is optimized for a CC mode charging current of 25A which translates to a peak output power of 10kW. The converter's maximum switching frequency is chosen as 200kHz. For efficient operation, the converter also needs to maintain ZVS of primary-side switches and ZCS of secondary-side diodes throughout the load range.

4.1 Design Approach

Since closed-form solutions were not possible for the proposed model, a grid search-based approach was used to highlight the power density vs efficiency trade-off when phase-shift modulation is used as an additional degree of freedom to regulate the output voltage gain. The design variables are $f_{n,min}$, L_r, C_r and L_m. The converter's maximum gain is determined by $f_{n,min}$ and thus it also determines the transformer turns ratio. The required voltage gain range of $[0.65, 1]$, output current of 25A and maximum switching frequency of 200kHz, which is also the resonant frequency, are equality constraints. As discussed in Chapter II, the inductor rms current acts as a surrogate variable for losses in the converter. The average value of rms current over the entire output voltage range is calculated for different designs to optimize the converter over the entire CC charging mode. The capacitor peak energy over the entire load range along with $f_{n,min}$ act as surrogate variables for the

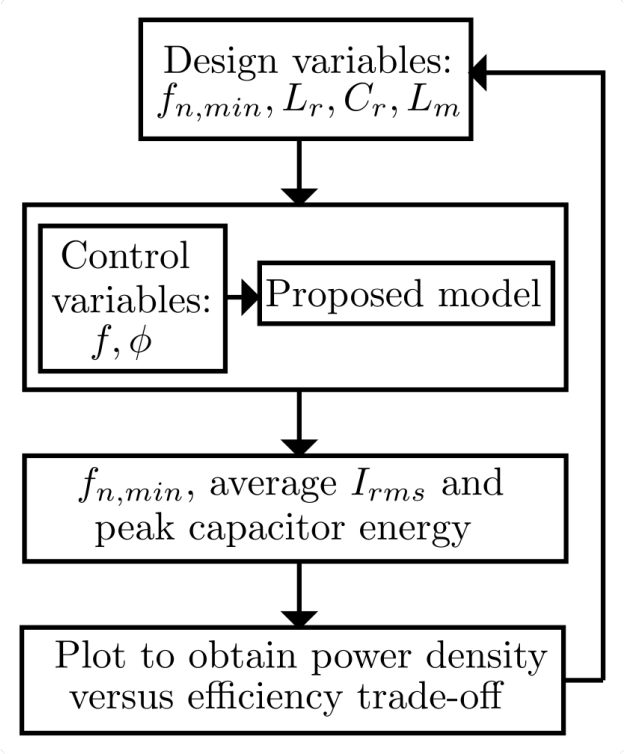

Figure 4.1: Design flowchart: control variables are changed to meet the equality constraints and surrogate variables for power density and efficiency are plotted for each design to obtain the trade-off curve.

size of the capacitor and transformer, respectively, for a particular design. The worst operating point from the transformer size standpoint is when the converter is operating at $f_{n,min}$, as the switching frequency is at its minimum and the converter gain at its maximum. The area product for the transformer is given by

$$A_{core}A_{copper} = \frac{\mathrm{VA}_{rated}}{2f_{n,min}k_w J B_m} \tag{4.1}$$

where VA_{rated} is the rated volt-amperes of the transformer, k_w is the winding fill factor, J is the current density of the copper, and B_m is the maximum flux density. The transformer size is reduced as $f_{n,min}$ is increased for a given VA_{rated}. However, this comes at the cost of a smaller peak gain from the converter. Phase-shift modulation must be used to achieve the required gain range. The design procedure is illustrated in Fig. 4.1. Figure 4.2 shows the capacitor peak energy and $f_{n,min}$ versus average I_{rms} over the entire load range for different design points. A minimum normalized frequency of 0.6,

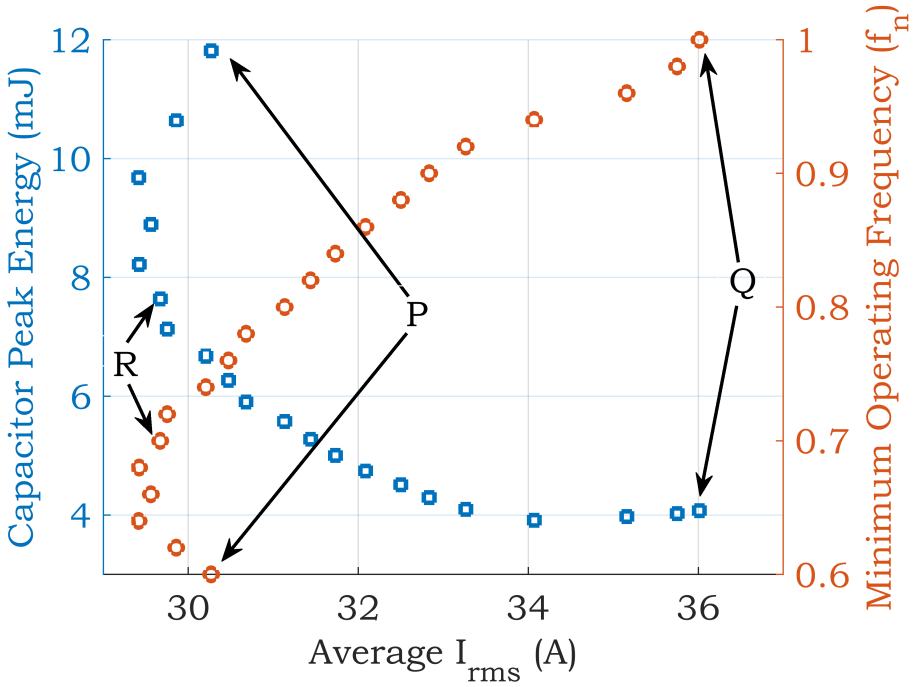

Figure 4.2: Capacitor peak energy (blue squares) and minimum operating normalized frequency (orange circles) versus the average value of inductor rms current over the entire CC mode.

marked by point P, allows frequency modulation alone to meet the output voltage gain constraint. A higher normalized minimum frequency requires both frequency and phase-shift modulation. As evident from the figure, if we rely solely on phase-shift modulation, marked by point Q, the capacitor and transformer size go down, but the average inductor rms current increases, thereby increasing losses. The trade-off curve conveys that for a minimum normalized frequency of 0.7, marked by point R, the average inductor rms current remains almost the same as frequency-only modulation but capacitor peak energy and transformer size go down. This implies that phase-shift modulation in conjunction with frequency modulation can be used to increase the overall power density without losing efficiency.

4.2 Comparison of the proposed model with FHA

Figures 4.3 and 4.4 compare the inductor rms current and capacitor peak voltage estimated using the proposed model to that obtained using FHA re-

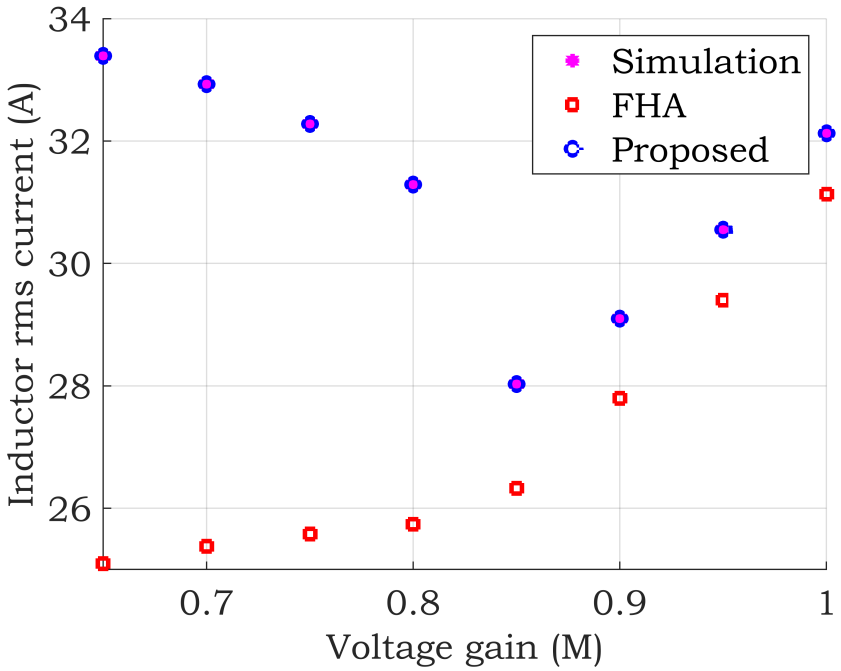

Figure 4.3: Inductor rms current for different output voltage gain for $V_{in} = 400V$, $L_r = 3.5\mu H$, $C_r = 180nF$, $n = 7/6$, $I_{load} = 25A$ as predicted by simulation (pink stars), FHA (red squares) and the proposed model (blue circles).

spectively. The predicted value from FHA-based analysis for both capacitor peak voltage and inductor rms current is considerably smaller when phase-shift modulation is used. Any design that incorporates phase-shift modulation based on FHA will underestimate the conduction losses and capacitor voltage rating. This might lead to capacitor failure due to overvoltage and overheating of the devices due to unaccounted losses.

4.3 Comparison with existing LLC-based converter designs for wide output voltage range

Table 4.1 compares the proposed design to existing LLC-based converter designs reported in the literature that achieve similar wide conversion ratios. The publications do not provide all of the relevant experimental data for a direct comparison so the designs are simulated using PLECS to obtain the capacitor peak voltage, inductor rms current, MOSFET peak blocking voltage,

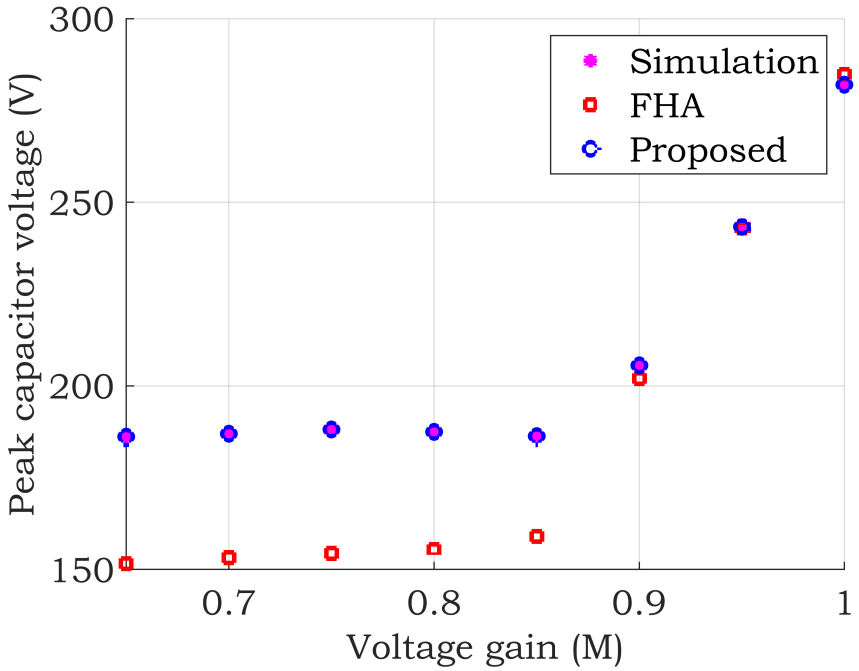

Figure 4.4: Capacitor peak voltage for different output voltage gain for $V_{in} = 400V$, $L_r = 3.5\mu H$, $C_r = 180nF$, $n = 7/6$, $I_{load} = 25A$ as predicted by simulation (pink stars), FHA (red squares) and the proposed model (blue circles).

and rms current, and diode peak blocking voltage and average current. The converters are compared using the operating frequency range, energy stored in the capacitor and inductor, and switch VA ratings. While the operating frequency range and energy stored in the resonant tank elements influence the size of the converter, the switch VA rating captures the loss in the converter. Energy stored in the capacitor and energy stored in the inductor is normalized to the total energy transferred to the load in one switching time period. The normalized energy stored in the capacitor is computed using

$$\text{Normalized energy in the capacitor} = \frac{\frac{1}{2}CV_{peak}^2}{\frac{P_{rated}}{f_{min}}} \tag{4.2}$$

where V_{peak} is the peak voltage across the capacitor, P_{rated} is the rated power of the converter, and f_{min} is the minimum operating switching frequency.

Similarly, the normalized energy stored in the inductor is calculated by

$$\text{Normalized energy in the inductor} = \frac{\frac{1}{2}LI_{rms}^2}{\frac{P_{rated}}{f_{min}}} \tag{4.3}$$

where I_{rms} is the maximum rms current through the inductor across the entire output voltage range.

Table 4.1: Comparison with existing LLC-based converters with wide output voltage range

	[9]	[10]	[14]	[23]	[28]	This work
Input voltage	400V	390V	400V	390V	390V	370V
Output voltage	250-420V	250-450V	250-400V	250-420V	150-420V	260-400V
Resonant inductor	26.5μH	15.3μH	2×13.5μH	28.1μH	2×28.1μH	3.4μH
Resonant capacitor	42.9nF	68.2nF	81.6nF	90nF	2× 90nF	169.9nF
Number of transformer	1	1	2	1	2	1
Power level	3.3kW	6.6kW	3.2kW	1kW	1kW	10kW
Frequency range	81.7-149.3kHz	85-200kHz	71-278kHz	100kHz	100kHz	145-209kHz
Normalized energy in the capacitor	0.207	0.32	0.167	0.04	1.44	0.134
Normalized energy in the inductor	0.034	0.04	0.025	0.02	0.05	0.023
Normalized switch VA rating	5.5	5.36	5.25	7.8	6.6	5.19

The normalized metric is based on I_{rms} rather than I_{peak} since not all the designs use soft magnetic materials for the inductor core. The size of inductors with the soft magnetic core is limited by core saturation which depends on I_{peak} whereas air core inductors are limited by losses which depend on I_{rms}. It should be noted that if I_{peak} was used instead, the normalized metric would be higher.

The normalized switch VA rating is computed by

$$\text{Normalized switch VA rating} = \frac{\begin{array}{r} N_{sw}V_{sw,rated}I_{sw,rms} \\ + N_dV_{d,rated}I_{d,avg} \end{array}}{P_{rated}} \tag{4.4}$$

where N_{sw} and N_d are the number of MOSFETs and number of diodes respectively, $V_{sw,rated}$ and $V_{d,rated}$ are the blocking voltages of the MOSFET and the diode, respectively, $I_{sw,rms}$ is the maximum rms current through the switch, and $I_{d,avg}$ is the average current through the diode. Conduction loss in MOSFETs is given by $I^2_{sw,rms} * R_{ds,on}$, which depends on rms current. Similarly, the conduction loss in diodes is given by $V_f * I_{d,avg}$, which depends on the average current.

Table 4.1 shows that the converter designed using the proposed approach has lower energy stored in the resonant tank elements, lower switch VA rating, and reduced operating frequency range compared to [9, 10, 28]. Although the switch VA rating and normalized inductor energy in [14] are comparable to the proposed design, the operating frequency range is increased by 2.8X, which will increase the transformer size. Moreover, this baseline design also has 24.6% higher normalized energy in the capacitor. Reference [23] employs only phase-shift modulation for output voltage regulation. This particular design allows a drastic reduction in the capacitor energy storage requirement at the cost of an increase in the rms current, as observed at the design point Q in Fig. 4.2. It remains at the designer's discretion to pick the final design from the trade-off curve of Fig. 4.2, based on the power density and efficiency targets.

CHAPTER 5

EXPERIMENTAL VERIFICATION

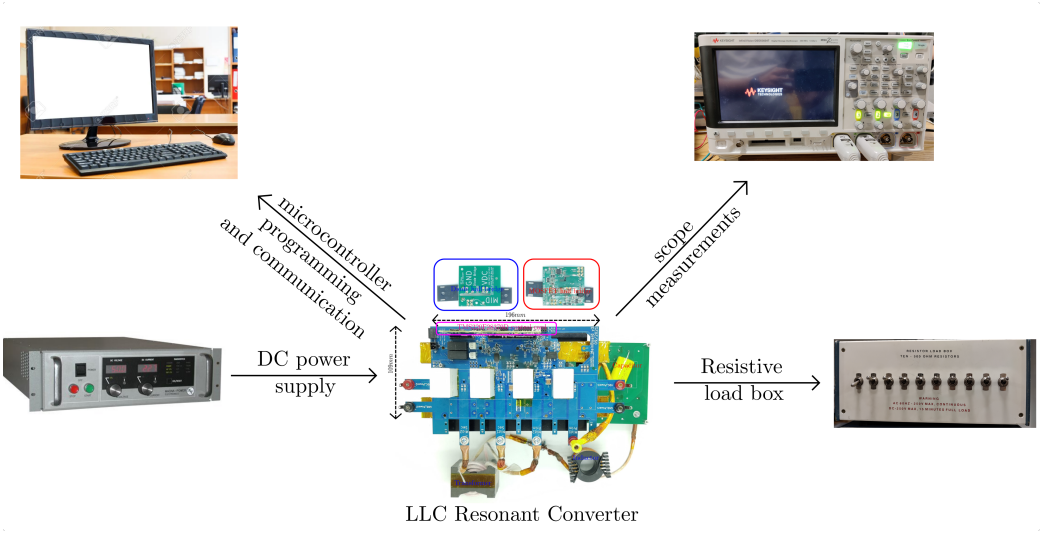

Figure 5.1: Experimental setup of the 10kW prototype converter. The converter is modular and the half bridges attach to the bottom of the PCB.

Two 10kW hardware prototypes are designed with a minimum normalized frequency of 0.6 and 0.7 to validate the results of the design process. The converter parameters and the selected components are listed in Table 5.1. The input voltage in the experiment is 370V and the peak output current is limited to 23A because of laboratory power supply constraints. The

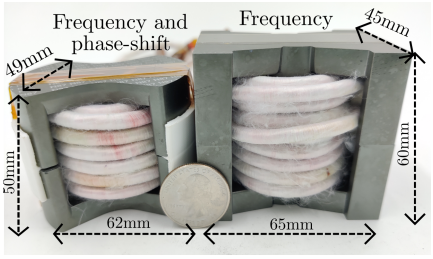

Figure 5.2: Size comparison of the transformer for frequency and phase-shift modulated (left) and frequency-only modulated (right) designs.

Table 5.1: Parameters and component list for frequency and phase-shift modulated, and frequency only modulated designs

Parameters	**Frequency + phase-shift**	**Frequency**
Input voltage	370V	370V
Output voltage range	260V to 400V	260V to 400V
Output current	23A	23A
Resonant frequency	209.4kHz	206.3kHz
Operating frequency range	145kHz to 209kHz	120kHz to 206kHz
Magnetizing inductance	24.8μH	25.9μH
Resonant inductor	3.4μH	3.5μH
Resonant capacitor	169.9nF	169.9nF
Capacitor peak voltage	330V	430V
Transformer Core	B65686A0000R087	B65982Q0250K097
Primary-side MOSFETs	IMZA65R027M1H	IMZA65R027M1H
Secondary-side Diodes	MSC050SDA070B	MSC050SDA070B

converter uses phase-shift control to reduce the operating frequency range. This results in a transformer that occupies 22% less space and has 28% less weight compared to a design using only frequency modulation for control. The transformer size comparison is shown in Fig. 5.2. The peak energy stored in the resonant capacitor is reduced by a factor of 1.7x, decreasing the size of the required resonant capacitor. The 10kW prototype converter is shown in Fig. 5.1.

5.1 Output Voltage Gain Characteristics

The experimental results are compared with the analytical model and simulation in PLECS to verify the accuracy of the proposed model. Figure 5.3 and 5.4 compares the output voltage gain obtained from the model, simulation, and experimental results. The switching frequency is varied from 145 kHz (f_n=0.69) to 209 kHz (f_n=1) and the phase-shift is varied from 0.55π to π respectively for a constant load current of 23A. As can be seen from

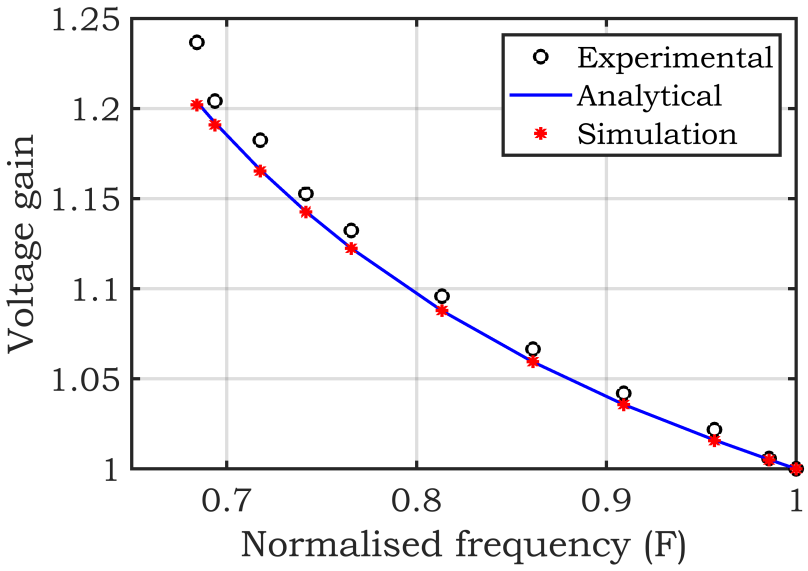

Figure 5.3: Output voltage gain with normalized frequency at a load current of 23A

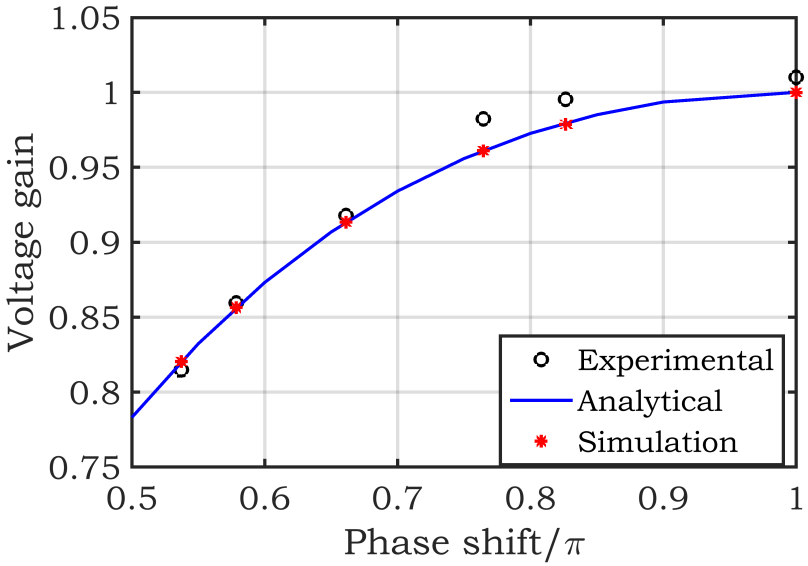

Figure 5.4: Output voltage gain with phase-shift at the resonant frequency at a load current of 23A

the plot, the analytical model matches exactly with the simulation results and tracks the experimental results very closely. Minor discrepancies can be attributed to drops across the diode, the MOSFET's on-state resistance, and resistance due to the transformer winding, capacitor ESR and PCB traces.

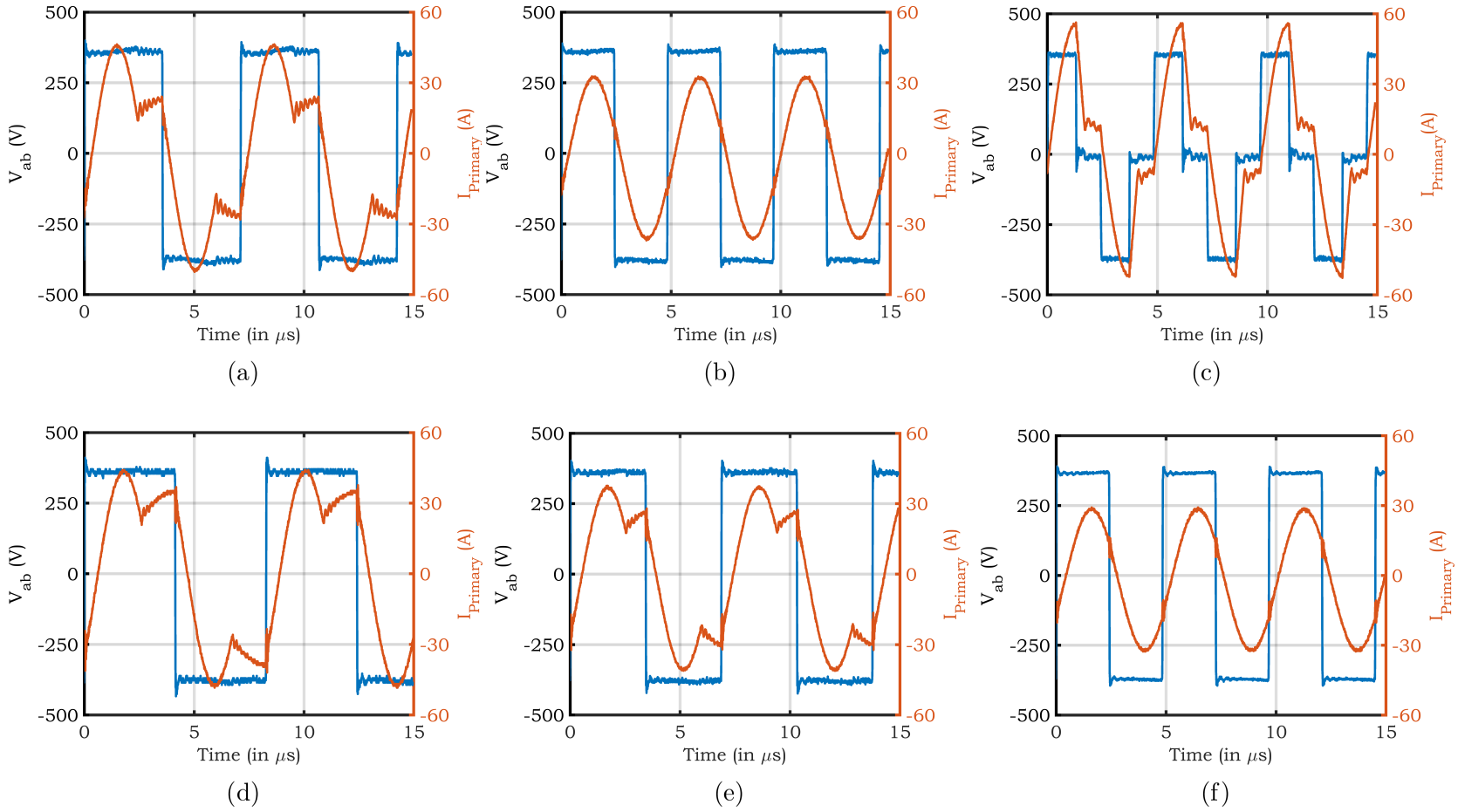

Figure 5.5: Operational waveforms for both frequency and phase shift modulated design at a load current of 23A and output voltages of (a) 400V, (b) 325V, and (c) 260V. Waveforms for only frequency modulated design at the same load current of 23A and output voltages of (d) 400V, (e) 325V, and (f) 260V.

5.2 Comparing the two designed converters

The main waveforms for the two designed converters are shown in Fig. 5.5. Both converters achieve ZVS throughout the operating range. Ringing in the inductor current is observed due to the parasitic capacitance of the rectifier diodes. Figure 5.5c experimentally demonstrates that the inductor current drops sharply when input to the resonant tank is effectively shorted. The current is not sinusoidal, which makes the first harmonic approximation unreliable for phase-shift modulation.

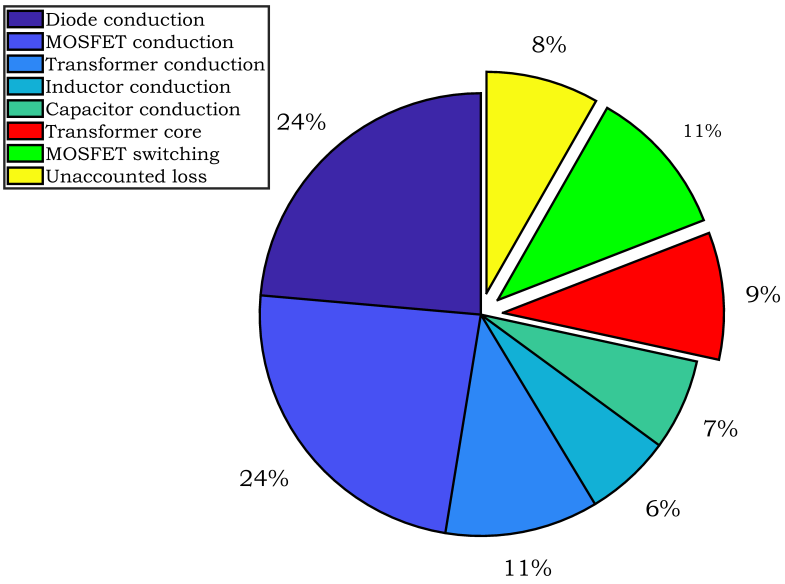

Figure 5.6: Loss distribution at peak load for combined frequency and phase-shift modulated converter were total loss = 264.7W.

The loss distribution at rated load for frequency and phase-shift modulated design is shown in Fig. 5.6. MOSFET conduction loss is calculated using the experimental value of rms current and on resistance obtained from the datasheet [32]. Diode loss is calculated using diode current and the forward voltage drop is given in the datasheet [33]. Transformer core loss is estimated using the Steinmetz equation [31]. Conduction losses in the inductor, transformer, and capacitor are calculated using the respective rms currents, and the resistance is measured at the switching frequency using HP 4284A precision LCR meter. MOSFET turn-off loss is calculated by measuring experimental fall time, dc link voltage, and current through the switch

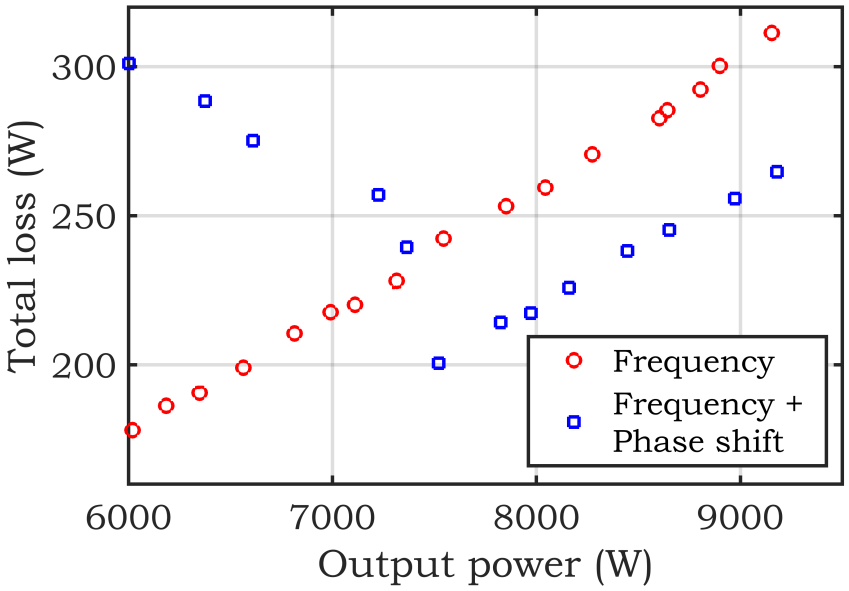

(a)

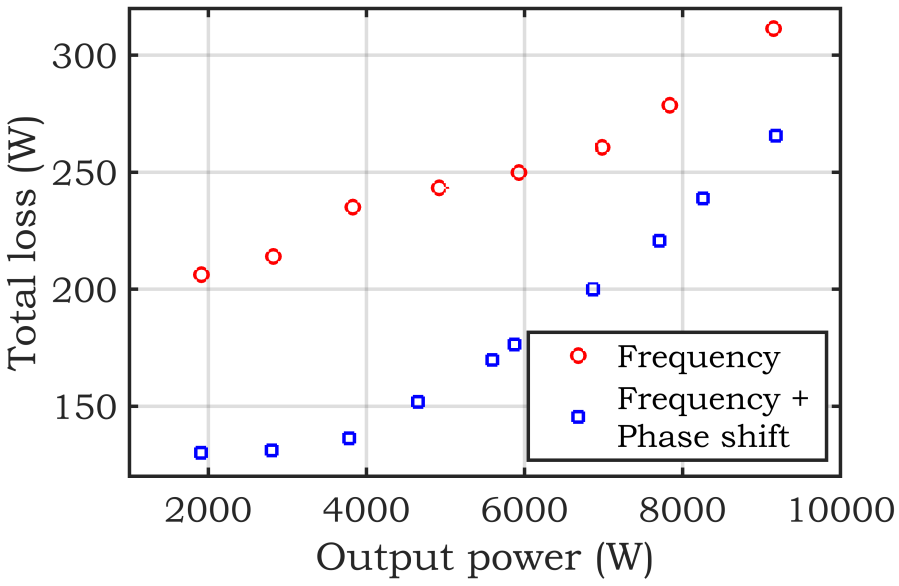

(b)

Figure 5.7: Total power loss in (a) CC mode with a constant load current of 23A and (b) CV mode with a constant output voltage of 400V.

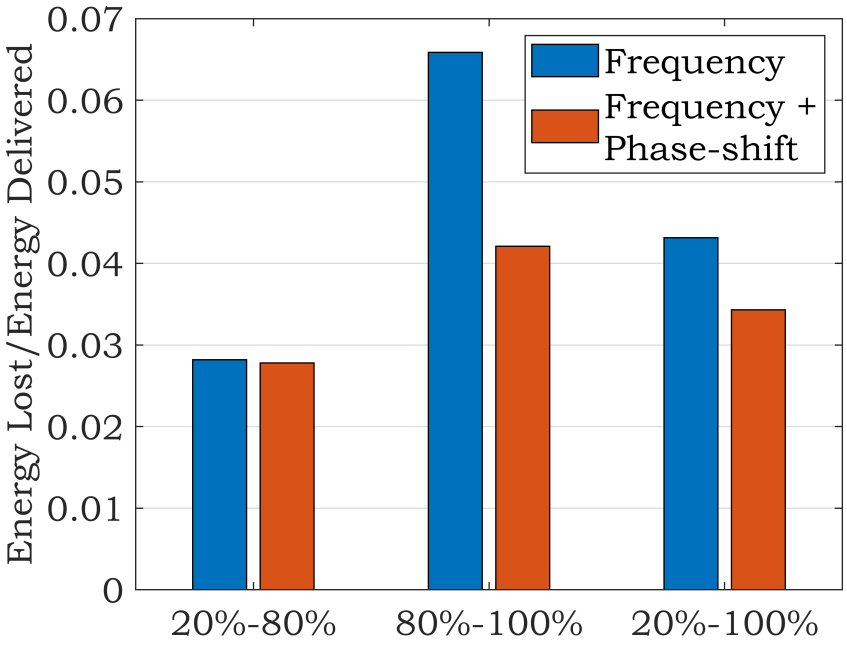

Figure 5.8: Energy lost / Energy delivered for frequency modulated and frequency and phase-shift modulated converter over different charging cycles.

during the turn-off transient. Total loss is calculated using keysight integravision power analyzer PA2201A. Seventy-two percent of the total loss is due to the conduction loss in different circuit elements. This experimentally validates the approach of using inductor rms current as a surrogate variable for efficiency.

The loss profiles of both converters are significantly different in CC charging mode as shown in Fig. 5.7a, due to different modulation techniques being used. However, they both have almost the same average power loss over the operating regime at 244.8W and 244.2W for the frequency-only modulated design and the frequency and phase-shift modulated design, respectively. The peak losses which determine the size of the heat sink needed are also similar at 311W and 301W for the frequency-only modulated design and the frequency and phase-shift modulated design, respectively. But, the frequency and phase-shift modulated converter incur significantly less loss in the constant voltage (CV) charging mode as shown in Fig. 5.7b. This reduction in loss happens because the rated voltage is achieved at a higher switching frequency in the frequency and phase-shift modulated converter which re-

duces circulating current and, therefore, reduces the conduction losses. The overall energy loss over different charging cycles is shown in Fig. 5.8. It is clear that both the frequency-modulated and frequency and phase-shift modulated converters have the same loss in 20%–80% charging cycle but the frequency and phase-shift modulated converter has 36% and 20.5% less loss for 80%–100% and 20%–100% charging cycles, respectively.

CHAPTER 6

CONCLUSION AND FUTURE WORK

6.1 Conclusion

In this thesis, the state plane approach is used to analytically model the LLC resonant converter in the DCM operating mode for both frequency and phase-shift modulation. The proposed approach is used to design an LLC resonant converter for EV battery charging applications which can achieve the required output voltage regulation with the reduced operating frequency range and reduced capacitor peak energy. This reduces both the transformer and the resonant capacitor size while achieving the same average efficiency in CC charging mode and incurring fewer losses in CV charging mode. Two 10kW SiC-based hardware prototypes are built, one uses frequency modulation alone for regulating output voltage, and the other both frequency and phase-shift modulation. The proposed model's accuracy is validated by the experimental and simulation results. The volumetric size of the transformer is reduced by 22%, and the weight is lowered by 28%. The capacitor peak energy storage requirement shrunk by 1.7x. The losses over the 20%–80% charging cycle remain the same but the frequency and phase-shift modulated design has 36% and 20.5% less loss over 80%–100% and 20%–100% charging cycles respectively.

6.2 Future Work

Possible future work is listed below:

- Developing fast control algorithms with high input disturbance rejection can allow for reduced input filter size further improving the power density of the converter
- Circuit changes by introducing additional switches and capacitors to shape the resonant tank current as a hybrid between a sinusoid and a trapezoid will lead in reduction of rms tank current while maintaining soft switching properties. This would enhance the efficiency of the dc-dc converter stage.
- The input dc link was assumed to be constant in this design procedure. Complete system-level design optimization with a variable dc-link after the PFC with a high bandwidth controller will lead to a further increase in the efficiency of the charging circuit

REFERENCES

[1] Z. Fang, T. Cai, S. Duan and C. Chen, "Optimal Design Methodology for LLC Resonant Converter in Battery Charging Applications Based on Time-Weighted Average Efficiency," in IEEE Transactions on Power Electronics, vol. 30, no. 10, pp. 5469-5483, Oct. 2015.

[2] F. Musavi, M. Craciun, D. S. Gautam, W. Eberle and W. G. Dunford, "An LLC Resonant DC–DC Converter for Wide Output Voltage Range Battery Charging Applications," in IEEE Transactions on Power Electronics, vol. 28, no. 12, pp. 5437-5445, Dec. 2013.

[3] F. Jin, A. Nabih, C. Chen, X. Chen, Q. Li and F. C. Lee, "A High Efficiency High Density DC/DC Converter for Battery Charger Applications," 2021 IEEE Applied Power Electronics Conference and Exposition (APEC), 2021, pp. 1767-1774.

[4] B. Li, Q. Li and F. C. Lee, "High-Frequency PCB Winding Transformer with Integrated Inductors for a Bi-Directional Resonant Converter," in IEEE Transactions on Power Electronics, vol. 34, no. 7, pp. 6123-6135, July 2019.

[5] C. -Y. Tang, H. -J. Wu, C. -Y. Liao and H. -H. Wu, "An Optimal Frequency-Modulated Hybrid MPPT Algorithm for the LLC Resonant Converter in PV Power Applications," in IEEE Transactions on Power Electronics, vol. 37, no. 1, pp. 944-954, Jan. 2022, doi: 10.1109/TPEL.2021.3094676.

[6] Q. Zhang et al., "A Center Point Iteration MPPT Method With Application on the Frequency-Modulated LLC Microinverter," in IEEE Transactions on Power Electronics, vol. 29, no. 3, pp. 1262-1274, March 2014, doi: 10.1109/TPEL.2013.2262806.

[7] Y. Wang, Y. Guan, K. Ren, W. Wang and D. Xu, "A Single-Stage LED Driver Based on BCM Boost Circuit and *LLC* Converter for Street Lighting System," in IEEE Transactions on Industrial Electronics, vol. 62, no. 9, pp. 5446-5457, Sept. 2015, doi: 10.1109/TIE.2015.2416341.

[8] H. Ma, Y. Li, Q. Chen, L. Zhang and J. Xu, "A Single-Stage Integrated Boost-LLC AC–DC Converter With Quasi-Constant Bus Voltage for Multichannel LED Street-Lighting Applications," in IEEE Journal of Emerging and Selected Topics in Power Electronics, vol. 6, no. 3, pp. 1143-1153, Sept. 2018, doi: 10.1109/JESTPE.2018.2847327.

[9] J. Deng, S. Li, S. Hu, C. C. Mi and R. Ma, "Design Methodology of LLC Resonant Converters for Electric Vehicle Battery Chargers," in IEEE Transactions on Vehicular Technology, vol. 63, no. 4, pp. 1581-1592, May 2014, doi: 10.1109/TVT.2013.2287379.

[10] J. Deng, C. C. Mi, R. Ma and S. Li, "Design of LLC Resonant Converters Based on Operation-Mode Analysis for Level Two PHEV Battery Chargers," in IEEE/ASME Transactions on Mechatronics, vol. 20, no. 4, pp. 1595-1606, Aug. 2015, doi: 10.1109/TMECH.2014.2349791.

[11] D. Kim, M. Kim and B. Lee, "An Integrated Battery Charger With High Power Density and Efficiency for Electric Vehicles," in IEEE Transactions on Power Electronics, vol. 32, no. 6, pp. 4553-4565, June 2017, doi: 10.1109/TPEL.2016.2604404.

[12] H. -I. Hsieh, H. Wang and T. -H. Huang, "LLC Charger Using Quasi-Contactless Power Transfer by Resonant Magnetic Induction Coupling," in IEEE Transactions on Transportation Electrification, vol. 4, no. 2, pp. 376-388, June 2018, doi: 10.1109/TTE.2018.2817125.

[13] H. -I. Hsieh and H. -W. Chen, "Ripple Behavior of LLC EV Charger in Boost Mode With Two-Capacitor Series Filter," in IEEE Transactions on Transportation Electrification, vol. 8, no. 1, pp. 830-844, March 2022, doi: 10.1109/TTE.2021.3110890.

[14] L. A. D. Ta, N. D. Dao and D. Lee, "High-Efficiency Hybrid LLC Resonant Converter for On-Board Chargers of Plug-In Electric Vehicles," in IEEE Transactions on Power Electronics, vol. 35, no. 8, pp. 8324-8334, Aug. 2020, doi: 10.1109/TPEL.2020.2968084..

[15] X. Rui, H. Hongwen, S. Fengchun and Z. Kai, "Evaluation on state of charge estimation of batteries with adaptive extended Kalman filter by experiment approach", IEEE Trans. Veh. Technol., vol. 62, no. 1, pp. 108-117, Jan. 2013.

[16] S. M. S. I. Shakib and S. Mekhilef, "A Frequency Adaptive Phase Shift Modulation Control Based LLC Series Resonant Converter for Wide Input Voltage Applications," in IEEE Transactions on Power Electronics, vol. 32, no. 11, pp. 8360-8370, Nov. 2017, doi: 10.1109/TPEL.2016.2643006.

[17] Y. Chen, J. Xu, Y. Gao, L. Lin, J. Cao and H. Ma, "Analysis and Design of Phase-Shift Pulse-Frequency-Modulated Full-Bridge LCC Resonant Converter," in IEEE Transactions on Industrial Electronics, vol. 67, no. 2, pp. 1092-1102, Feb. 2020, doi: 10.1109/TIE.2019.2898586.

[18] A. Mustafa and S. Mekhilef, "Dual Phase LLC Resonant Converter With Variable Frequency Zero Circulating Current Phase-Shift Modulation for Wide Input Voltage Range Applications," in IEEE Transactions on Power Electronics, vol. 36, no. 3, pp. 2793-2807, March 2021, doi: 10.1109/TPEL.2020.3015799.

[19] H. Park and J. Jung, "PWM and PFM Hybrid Control Method for LLC Resonant Converters in High Switching Frequency Operation," in IEEE Transactions on Industrial Electronics, vol. 64, no. 1, pp. 253-263, Jan. 2017, doi: 10.1109/TIE.2016.2599138.

[20] J. Jiao, X. Guo, C. Wang and X. You, "Time-Domain Analysis and Optimal Design of LLC-DC Transformers (LLC-DCXs) Considering Discontinuous Conduction Modes," in IEEE Transactions on Transportation Electrification, 2022, doi: 10.1109/TTE.2022.3205954.

[21] A. Awasthi, S. Bagawade and P. K. Jain, "Analysis of a Hybrid Variable-Frequency-Duty-Cycle-Modulated Low-Q LLC Resonant Converter for Improving the Light-Load Efficiency for a Wide Input Voltage Range," in IEEE Transactions on Power Electronics, vol. 36, no. 7, pp. 8476-8493, July 2021, doi: 10.1109/TPEL.2020.3046560.

[22] U. Mumtahina and P. J. Wolfs, "Multimode Optimization of the Phase-Shifted LLC Series Resonant Converter," in IEEE Transactions on Power Electronics, vol. 33, no. 12, pp. 10478-10489, Dec. 2018, doi: 10.1109/TPEL.2018.2803741.

[23] H. Wang and Z. Li, "A PWM LLC Type Resonant Converter Adapted to Wide Output Range in PEV Charging Applications," in IEEE Transactions on Power Electronics, vol. 33, no. 5, pp. 3791-3801, May 2018, doi: 10.1109/TPEL.2017.2713815.

[24] Liu, S. and Zhang, F. (2019), State variable derivation with numerical approach and efficiency optimisation method for phase-shift LLC converters under wide voltage-gain range. IET Power Electronics, 12: 1752-1762. https://doi.org/10.1049/iet-pel.2018.5213

[25] L. Shi, B. Liu and S. Duan, "Burst-Mode and Phase-Shift Hybrid Control Method of LLC Converters for Wide Output Range Applications," in IEEE Transactions on Industrial Electronics, vol. 67, no. 2, pp. 1013-1023, Feb. 2020, doi: 10.1109/TIE.2019.2898578.

[26] H. Wu, X. Zhan and Y. Xing, "Interleaved LLC Resonant Converter With Hybrid Rectifier and Variable-Frequency Plus Phase-Shift Control for Wide Output Voltage Range Applications," in IEEE Transactions on Power Electronics, vol. 32, no. 6, pp. 4246-4257, June 2017, doi: 10.1109/TPEL.2016.2602545.

[27] J. Kim, C. Kim, J. Kim, J. Lee and G. Moon, "Analysis on Load-Adaptive Phase-Shift Control for High Efficiency Full-Bridge LLC Resonant Converter Under Light-Load Conditions," in IEEE Transactions on Power Electronics, vol. 31, no. 7, pp. 4942-4955, July 2016, doi: 10.1109/TPEL.2015.2462077.

[28] B. Xue, H. Wang, J. Liang, Q. Cao and Z. Li, "Phase-Shift Modulated Interleaved LLC Converter With Ultrawide Output Voltage Range," in IEEE Transactions on Power Electronics, vol. 36, no. 1, pp. 493-503, Jan. 2021, doi: 10.1109/TPEL.2020.3001126.

[29] Y. Shen, H. Wang, F. Blaabjerg, X. Sun and X. Li, "Analytical model for LLC resonant converter with variable duty-cycle control," 2016 IEEE Energy Conversion Congress and Exposition (ECCE), 2016, pp. 1-7, doi: 10.1109/ECCE.2016.7854882.

[30] RW Erickson and D Maksimovic, "Fundamentals of power electronics," Springer Science & Business Media, 2007.

[31] "Core Loss Datasheet - MnZn Ferrite - N87." [Online]. Available: https://www.netl.doe.gov/sites/default/files/netl-file/Core-Loss-Datasheet—MnZn-Ferrite—N87%5B1%5D.pdf

[32] "Datasheet IMZA65R027M1H" [Online]. Available: https://www.mouser.com/datasheet/2/196/Infineon-IMZA65R027M1H-DataSheet-v02_00-EN-1840512.pdf

[33] "Microsemi MSC050SDA070B" [Online]. Available: https://www.mouser.com/datasheet/2/268/Microsemi_MSC050SDA070B_Datasheet-2934462.pdf

APPENDIX A

MATHEMATICAL PROPERTIES OF CIRCLES

A.1 Average value of y coordinate in a circular trajectory

The average of the y coordinate for an arc of a circle spanned by coordinates (x_1, y_1) and (x_2, y_2) centered at the origin is

$$< y >= \frac{1}{\theta_2 - \theta_1}(\int_{\theta_1}^{\theta_2} y d\theta) \tag{A.1}$$

where θ_1 and θ_2 are the counter-clockwise angles made by the positive x-axis and the lines joining the origin with (x_1, y_1) and (x_2, y_2) respectively. Substituting $y = rsin(\theta)$ in the above equation where r is the radius of the circle, we get

$$\begin{aligned} < y > &= \frac{1}{\theta_2 - \theta_1}(\int_{\theta_1}^{\theta_2} rsin(\theta) d\theta) \\ &= \frac{1}{\theta_2 - \theta_1}(-rcos(\theta_2) + rcos(\theta_1)) \\ &= \frac{1}{\theta_2 - \theta_1}(x_1 - x_2) \end{aligned} \tag{A.2}$$

A.2 RMS value of y coordinate in a circular trajectory

The rms of the y coordinate for an arc of a circle spanned by coordinates (x_1, y_1) and (x_2, y_2) centered at the origin is

$$y_{rms} = \frac{1}{\theta_2 - \theta_1}(\int_{\theta_1}^{\theta_2} y^2 d\theta) \tag{A.3}$$

where θ_1 and θ_2 are the counter-clockwise angles made by the positive x-axis and the lines joining the origin with (x_1, y_1) and (x_2, y_2) respectively. Substituting $y = rsin(\theta)$ in the above equation where r is the radius of the circle, we get

$$\begin{aligned} y_{rms} &= \sqrt{\frac{1}{\theta_2 - \theta_1}(\int_{\theta_1}^{\theta_2} r^2 sin^2(\theta) d\theta)} \\ &= \sqrt{\frac{1}{\theta_2 - \theta_1}(\int_{\theta_1}^{\theta_2} r^2 \frac{1 - cos(2\theta)}{2} d\theta)} \\ &= \sqrt{\frac{1}{2}(r^2 + r^2 \frac{sin(2\theta_2) - sin(2\theta_1)}{2(\theta_2 - \theta_1)})} \end{aligned} \tag{A.4}$$

Using trigonometric identity, $sin(2\theta) = 2sin(\theta)cos(\theta)$ and $rcos(\theta) = x$ and $rsin(\theta) = y$, we get

$$y_{rms} = \sqrt{\frac{1}{2}(r^2 + \frac{x_2 y_2 - x_1 y_1}{\theta_2 - \theta_1})} \tag{A.5}$$

APPENDIX B

DIFFERENT OPERATING MODES OF LLC RESONANT CONVERTER IN BELOW RESONANT FREQUENCY MODE

A total of eight different circuit states are possible, shown in Fig. 3.5. However, not all switching states will manifest themselves in a switching cycle. The states shown in Figs. 3.5(II), 3.5(III), 3.5(V), and 3.5(VI) only occur when phase-shift modulation is used.

1. State a: This state occurs when switches S1 and S4 are ON and diodes D1 and D4 are conducting. As a result, the voltage at the input of the resonant tank is $+V_{in}$, and the voltage across the magnetizing inductance is $+V_{out}$. The circuit diagram of this state is shown in Fig. 3.5(I). The effective voltage across the resonant tank is $V_{in} - V_{out}$. The state plane diagram in this state is a circle centered at (1-M, 0), where M is the converter's gain.

2. State b: This state occurs when switches S1 and S3 are ON and diodes D1 and D4 are conducting. As a result, the input of the resonant tank is shorted and the voltage across the magnetizing inductance is still $+V_{out}$. The circuit diagram of this state is shown in Fig. 3.5(II). The effective voltage across the resonant tank is $-V_{out}$. The state plane diagram in this state is a circle centered at (-M, 0).

3. State c: This state occurs when switches S1 and S3 are ON and none of the diodes are conducting. As a result, the input of the resonant tank is shorted and the magnetizing inductance joins the resonance. The circuit diagram of this state is shown in Fig. 3.5(III). The effective voltage across the resonant tank is 0. The state plane diagram in this state is an ellipse centered at the origin.

4. State d: This state occurs when switches S2 and S3 are ON and diodes D2 and D3 are conducting. As a result, the voltage at the input of

the resonant tank is $-V_{in}$, and the voltage across the magnetizing inductance is $-V_{out}$. The circuit diagram of this state is shown in Fig. 3.5(IV). The effective voltage across the resonant tank is $-V_{in} + V_{out}$. The state plane diagram in this state is a circle centered at (-1+M, 0), where M is the converter's gain.

5. State e: This state occurs when switches S2 and S4 are ON and diodes D2 and D3 are conducting. As a result, the input of the resonant tank is shorted and the voltage across the magnetizing inductance is still $-V_{out}$. The circuit diagram of this state is shown in Fig. 3.5(V). The effective voltage across the resonant tank is $+V_{out}$. The state plane diagram in this state is a circle centered at (M, 0).

6. State f: This state occurs when switches S2 and S4 are ON and none of the diodes are conducting. As a result, the input of the resonant tank is shorted and the magnetizing inductance joins the resonance. The circuit diagram of this state is shown in Fig. 3.5(VI). The effective voltage across the resonant tank is 0. The state plane diagram in this state is an ellipse centered at the origin.

7. State g: This state occurs when switches S1 and S4 are ON and none of the diodes are conducting. As a result, the input of the resonant tank is V_{in}, and the magnetizing inductance joins the resonance. The circuit diagram of this state is shown in Fig. 3.5(VII). The effective voltage across the resonant tank is V_{in}. The state plane diagram in this state is an ellipse centered at (1,0).

8. State h: This state occurs when switches S2 and S3 are ON and none of the diodes are conducting. As a result, the input of the resonant tank is $-V_{in}$, and the magnetizing inductance joins the resonance. The circuit diagram of this state is shown in Fig. 3.5(VIII). The effective voltage across the resonant tank is $-V_{in}$. The state plane diagram in this state is an ellipse centered at (-1,0).

APPENDIX C

PLECS SIMULATION MODEL

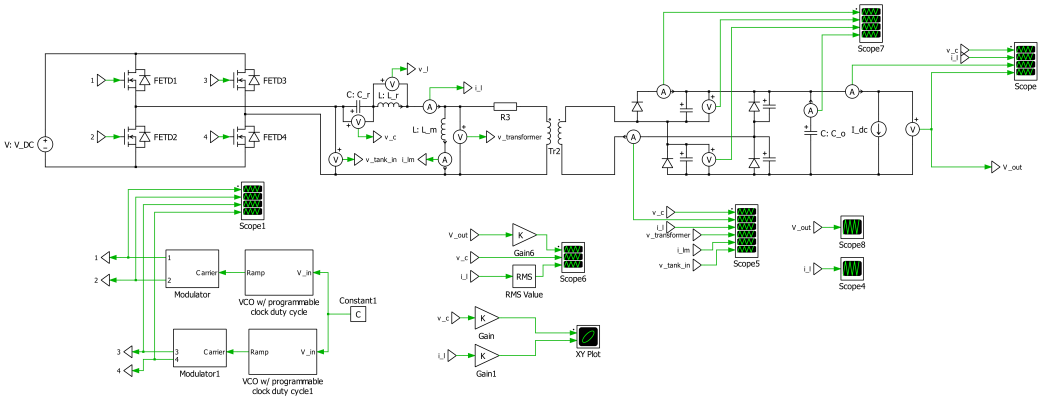

Figure C.1: Simulation model of LLC resonant converter in PLECS